X-Ray Optics on a Chip: Guiding X Rays in Curved Channels

T. Salditt,[1] S. Hoffmann,[1] M. Vassholz,[1] J. Haber,[2] M. Osterhoff,[1] and J. Hilhorst[3]
[1]*Institut für Röntgenphysik, Georg-August-Universität Göttingen, Friedrich-Hund-Platz 1, Göttingen, Germany*
[2]*DESY Photon Science, Hamburg, Germany*
[3]*European Synchrotron Radiation Facility, Grenoble, France*
(Received 13 July 2015; published 9 November 2015)

We study the propagation of hard x rays in single curved x-ray waveguide channels and observe waveguide effects down to surprisingly small radii of curvature $R \simeq 10$ mm and a large contour length $s \simeq 5$ mm, deflecting beams up to 30°. At these high angles, about 2 orders of magnitude above the critical angle of total reflection θ_c, most radiation modes are lost by "leaking" into the cladding, while certain "survivor" modes persist. This may open up a new form of integrated x-ray optics "on a chip," requiring curvatures mostly well below the extreme values studied here, e.g., to split and to delay x-ray pulses.

DOI: 10.1103/PhysRevLett.115.203902 PACS numbers: 42.81.−i, 07.85.−m, 41.50.+h, 42.82.Et

X-ray optics suffer from the fact that many optical elements that are routinely available in the visible spectrum are missing or difficult to realize in the spectral range of x rays. While recent progress in diffractive, refractive, as well as reflective optics has led to significant improvements in x-ray focusing [1,2], capabilities in fiber optics, interferometry, and the control of short pulses are still lacking. Current setups are based on multiple mirror [3], crystal [4], or grating reflections [5], which are used, for example, as beam splitters or delay lines in interferometry, pump probe experiments, or pulse length measurements [3,6]. Extending the optical functions of these macroscopic devices, x-ray integrated optics could provide a downscaled version of such optical setups and enable pulse splitting, delay lines, and interferometric manipulations at the nanometer and femtosecond scales. Such an "x-ray optics on a chip" approach could also encompass the handling of multiple beams, extending current interferometry or coherent x-ray imaging systems [7,8]. Integrated x-ray optics could be realized based on waveguide optics, serving, for example, novel applications with ultrashort Free Electron Laser pulses, from pulse length measurements to pump-probe experiments. Multibeam illumination systems for Free Electron Laser and synchrotron radiation, based on splitting and redirecting of beams in a waveguide chip, could also enable off-axis holography [9] or parallel recordings of several tomographic projections. Specially designed wave fronts and, in particular, wave fronts with high numerical aperture could be realized by combinations of several coherent beams emanating from a waveguide chip.

For such novel devices, a key ingredient is a curved segment of an x-ray waveguide channel. Guiding of x rays has been well studied theoretically and experimentally both for planar [10–12] and for channel waveguides [13–16], but curvature has not been addressed so far. Contrarily, for x-ray whispering gallery modes using bent silicon crystals, Liu and Golovchenko have already shown that x rays can be deflected at much larger angles than the critical angle θ_c of x-ray total reflection, which is in the mrad range for hard x rays [17]. In this work, we demonstrate hard x-ray propagation in curved lithographic waveguide channels, which are well suited for applications in x-ray integrated optics, reflecting the beam up to 30°. Waveguiding effects are evidenced in channels with radius of curvature $R[mm] \in 10, 20, 30, 40, 80$, i.e., at much higher curvature than would be required for most multibeam interferometry and imaging application. The increase in curvature and deflection angle is achieved by using small waveguide channels in combination with state-of-the-art x-ray focusing optics, based on Kirkpatrick-Baez mirrors (KB) or Fresnel zone plates (FZP). The focused synchrotron (undulator) beam is coupled into the front side of an x-ray waveguide chip (XWGchip). The XWGchip has multiple channels of different curvature and geometry, as defined by e-beam lithography. The exit radiation is recorded with pixel detectors, covering the direct and the redirected beams, respectively, in the far field, as well as leaky modes emitted along the contour of the curved channels.

Figure 1 shows a schematic of the XWGchip with a pattered area of 5×5 mm (xz plane) made of a 500-nm-thick Ta layer, in which a number of channels were defined by e-beam lithography. The defined pattern contains several undulating channels, split and delay lines, beam splitters, and the curved WG channels investigated here. With constant radius of curvature $R = 10, 20, 30, 40, 80$ mm and constant channel width $w = 100$ nm, the curved WG channels were arranged as indicated in (a). Along the vertical direction y, channels were open (no confinement by a cap wafer as in Ref. [15]). In (b), a wave-optical simulation of x-ray mode propagation by the finite difference method is shown for a curved channel with $R =$ 40 mm (air in Ta), for the experimental parameters $E =$ 7.9 keV and $w = 100$ nm. The region shown covers only

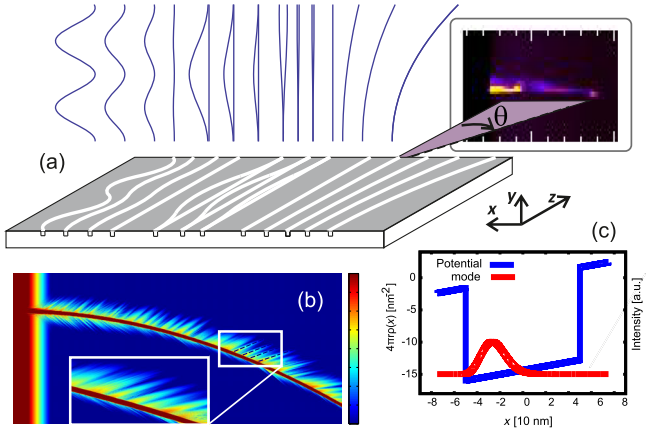

FIG. 1 (color online). (a) Schematic of the channels defined in the XWGchip and the experimental geometry. The individual channels are selected by focusing the beam into the entrance. Guiding of a beam in a curved channel is evidenced by measurement of the far-field pattern. (b) Finite difference simulation of beam propagation in the curved WG channels. At $z = 0$ a plane wave of unit amplitude and 7.9 keV photon energy impinges on a channel of $w = 100$ nm and $R = 40$ mm in Ta (initial data). The intensity distribution is shown in logarithmic scale within a rectangular region of length $\Delta z = 0.5$ mm and width $\Delta x = 5$ μm, along with a zoom of the central region with $\Delta z = 100$ μm and $\Delta x = 1.5$ μm. The transmission is $T = 0.842$, after a propagation length of 0.5 mm. The spikes show that evanescent waves depart into the cladding at certain locations corresponding to reflections in the geometric optical description. (c) Fundamental mode of a channel in tantalum (Ta) with $w =$ 100 nm and $R = 10$ mm as simulated by solving the wave equation with a tilted potential well.

the first 10% of the propagation in the XWGchip. Intensity is shown in logarithmic scaling to highlight the evanescent waves. Spikes are observed departing into the cladding. For Ta and the given channel width w, 13 bound modes copropagate in the channel. The fundamental mode as calculated in the effective tilted potential by Numerov's method [18] is shown in (c).

Experiments were first carried out at the GINIX nano-imaging end station [19] of the coherence beam line P10 at the storage ring PETRAIII (DESY, Hamburg), at photon energy of $E = 7.9$ keV. The monochromatic [Si(111) double crystal] undulator beam was focused with two elliptical total reflection mirrors in Kirkpatrick-Baez (KB) geometry, to a focus of 380 nm × 350 nm ($h \times v$, FWHM values) with a primary beam intensity of about $I_0 = 4.1 \times 10^{11}$ ph/s. The focused beam was coupled to selected channels of the XWGchip, aligned in the focal plane, and the far-field intensity of the exit radiation at the horizon of the chip was recorded by a PILATUS 100K, positioned at a distance of 348.8 mm. For full details on the experiment and the layout of the XWGchip, see Ref. [20]. With an index of refraction $n = 1 - \delta + i\beta$ for Ta of $\delta = 4.14 \times 10^{-5}$ and $\beta = 3.45 \times 10^{-6}$, a critical angle of total reflection $\alpha_c \simeq \sqrt{2\delta} = 9.1$ mrad and attenuation length $l = \lambda/(4\pi)/\beta = 3.62$ μm is obtained, such that the XWGchip of 5 mm length is completely intransparent for radiative modes. According to simple geometric optics, the condition that the incoming beam impinges at an angle of incidence $\alpha_i \le \alpha_c$ with respect to the outer channel wall gives a simple constraint for the radius of curvature $R \ge w/2\sin^2(\alpha_c/2) \simeq 2\pi w/(\lambda^2 r_0 \rho)$, with r_0 the Thompson scattering length and ρ the electron density.

To describe the mode propagation in a "potential well" given by the one-dimensional electron density profile function $\rho(x)$, we consider the reduced scalar wave equation $\psi'' - 4\pi r_0 \rho(x)\psi = (\beta^2 - k_0^2)\psi$ describing propagation of guided modes in a planar waveguide, with the mode number $M := \beta^2 - k_0^2$, depending on the solution of the corresponding eigenvalue problem. For the simple case relevant here, $\rho(x)$ is a rectangular profile with height ρ_0 and width w. The dimension of M is that of scattering length density. For the example of an air-vacuum channel in Ta, we get $4\pi r_0 \rho_0 = 0.144$ nm^{-2}.

How does the situation change for a curved channel? Following Ref. [21], translated to the case of x-ray notation, we get

$$\psi'' - \left(4\pi r_0 \rho(x) + \frac{2k_0^2 - 4\pi r_0 \rho(x)}{R} x\right)\psi = (\beta^2 - k_0^2)\psi, \quad (1)$$

where R is the radius of the curvature. The curvature-induced term leads to a distortion of the potential, notably a tilt. We can further neglect the ρ dependence in the curvature term $2k_0^2 - 4\pi r_0 \rho(x) \simeq 2k_0^2$, so that only a linear potential is added to the intrinsic waveguide potential,

$$\psi'' - \left(4\pi r_0 \rho(x) + \frac{2k_0^2}{R} x\right)\psi = (\beta^2 - k_0^2)\psi. \quad (2)$$

For $R(w) = 2\pi w/(\lambda^2 r_0 \rho)$, the tilt becomes so strong that the right side of the potential well (inner side wall of the curved channel) has the same height as the cladding potential on the left side. Hence, the confining potential has changed from a square to a triangular well, and the width of the barrier at the base of the well decreases to w. Interestingly, this transition corresponds exactly to the above geometric optical constraint. However, in wave optics we cannot reduce w arbitrarily in order to accommodate higher curvature. The minimum reasonable channel width is given by the critical waveguide thickness for single-mode propagation $W := \lambda/2\alpha_c = \sqrt{\pi/4\rho r_0}$. Upon further reduction $w < W$, the evanescent tails of the wave extend further into the cladding. and the beam cannot be further confined [22,23]. For Ta we have $W = 8.62$ nm, and hence, we obtain a critical radius $R_c = 8W^3/\lambda^2 = 0.21$ mm. For $R \le R_c$ the beam is lost by tunneling as the barrier of the potential well becomes too thin to guide radiation. Note that for $R \simeq R_c$ we estimate that the mode power is lost over a length given by w^2/λ, so that in

practice R has to exceed R_c by a factor of 1 or 2 orders of magnitude depending on the channel length L. Contrarily, for $R \gg R_c$ tunneling losses become negligible, and losses are dominated by absorption in the cladding, with the absorption coefficient depending on the mode number and on R. With decreasing R, a larger fraction of the wave is "pressed into" the cladding, and higher absorption can be expected. To obtain an order of magnitude estimate of the curvature-dependent attenuation length, we turn to finite difference simulations as illustrated in Fig. 1(b). The intensity distribution shows some curvature-induced leakage into the cladding (in logarithmic scale), but some modes persist over several mm-long path lengths as required for the XWGchip, even if R decreases down to the range $R = 40$–10 mm. Qualitatively speaking, the situation is as follows: The higher modes are lost due to tunneling out of the tilted potential, while the lower modes are well confined but exhibit a different mode function with an increased proportion of the field propagating in the outer cladding. This leads to a higher effective absorption coefficient μ_{eff} in the tilted (curved) than in the straight reference channel.

Figure 2 shows far-field patterns of curved WG channels, measured as a function of deflection angle θ as sketched in (a). The deflected WG beams that are coupled along the exit tangents of the curved waveguide are recorded with a pixel detector (Pilatus 100k, Dectris). The deflection angle θ of the exit beam increases as a function of curvature $1/R$ as expected for (b) $R = 10$ mm, (c) $R = 20$ mm, (d) $R = 40$ mm, and (e) $R = 80$ mm, in perfect agreement with the values expected from the geometric layout. The results show that significant intensities can be transported

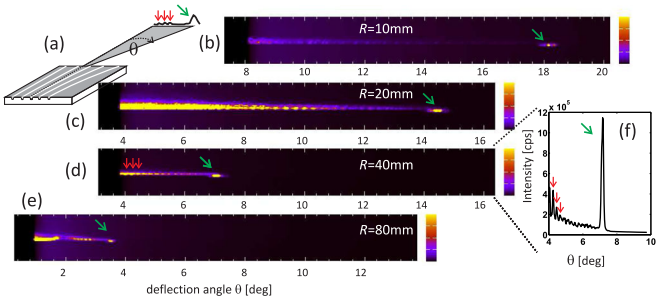

FIG. 2 (color online). Measured far-field patterns of the curved WG series. (a) Experimental geometry. Intensity distribution on the pixel detector moved out of the plane of incidence to record the exit WG beam at a deflection angle θ as given by the exit tangent of the curved channel, for channels with (b) $R = 10$ mm, (c) $R = 20$ mm, (d) $R = 40$ mm, and (e) $R = 80$ mm. Intensity due to radiation losses of leaky modes is observed along the entire horizon, but the propagating modes of the waveguide couple out only at the end of the 5-mm-long WG chip, leading to a pronounced peak in the WG pointing direction. (f) The intensity distribution after integration over the exit angle α_f, as a 1D plot for the example of the $R = 40$ mm guide shows that the exit peak of the transported modes is significantly higher than the radiation loss at smaller θ.

over several mm to exit at high angles, for example, 18.24° for the $R = 10$ mm guide, which exits at the side of the XWGchip. Along the horizon of the WGchip—tangentially to the curved WG channels—radiation corresponding to leaky modes is lost and decoupled at small exit angles $\alpha_f \simeq \alpha_c$. This leads to a horizontal stripe of radiation coupled vertically out of the uncapped channel, with a characteristic spike pattern also observed in the simulations, as indicated by the arrows.

Motivated by the positive results, the experiments were extended to a second chip (XWGchipII) with smaller radii of curvature $R[\mathrm{mm}] \in 1, 2, 3{,}4, 6, 10, 20, 30$, probed this time with an $E = 8$ keV undulator beam of the upgraded ID01 beam line at ESRF (Grenoble, France) (see Ref. [20] for details). For $R < L = 5$ mm the channels end at 90° at the side of the chip; for $R > L$ the channels exit at an angle $\theta_{\mathrm{max}} = \arcsin(5\ \mathrm{mm}/R)$. The beam was focused into the entrance of the channels by a Fresnel zone plate (FZP) to a focus of 525 nm × 171 nm (h × v, FWHM values), with a total intensity of $I_0 \simeq 0.80 - 3.25 \times 10^{10}$ ph/s, depending on the alignment conditions and ring current. The far-field diffraction patterns were recorded at high resolution with a pixel detector (Maxipix, ESRF) of 55 μm pixel size, mounted on a diffractometer at a distance of 750 mm. For the $R = 10$ mm channel, a waveguide exit intensity of $I_{\mathrm{WG}} = 1.9 \times 10^5$ ph/s was recorded, exiting at 30°. For $R = 6$ mm and below, radiation of leaky modes was observable up to $\theta \geq 35°$. No radiation was detected from the channel exit at 90°.

Figure 3 quantifies the leakage radiation and curved waveguide transmission. For the example of $R = 40$ mm, (a) shows the far field of the waveguided radiation (peak in right detector module), along with the radiation tunneling out of the "leaky" modes, visible as a horizontal stripe, similar to Fig. 2, but now recorded with higher angular resolution. Scanning the detector along the horizon, the leakage radiation was measured as a function of θ for different R [see (b)]. Since the loss rate can be assumed to be proportional to the local mode intensity, an exponential decay is expected, with a characteristic decay constant for each mode. Modes with high loss coefficients depopulate first, while "survivor" modes with smaller loss rates persist to higher θ, decaying with a reduced slope [see the two regimes for the $R = 3$ mm curve in (b)]. For a particular regime, given by a single mode or a band of modes with similar loss rate, the guided intensity can be written as a function of propagation length l as $I(l) \propto \exp[-l/(R\theta_{1/e})]$. Consider, for example, the decay constant $\theta_{1/e} = 2.2°$, fitted to the $R = 10$ mm curve in the range $16° \leq \theta \leq 29°$ (solid line). Based on this loss rate, one can expect a transmission of about $\simeq \exp(-130\ \mathrm{mm}/R)$ for a chip length of 5 mm. The $1/R$ dependence of the transmission is confirmed by comparison of the waveguide exit intensity I_{WG} for different R^{-1} [see (c)]. Values are plotted for both experiments (KB and FZP coupling), normalized to the flux

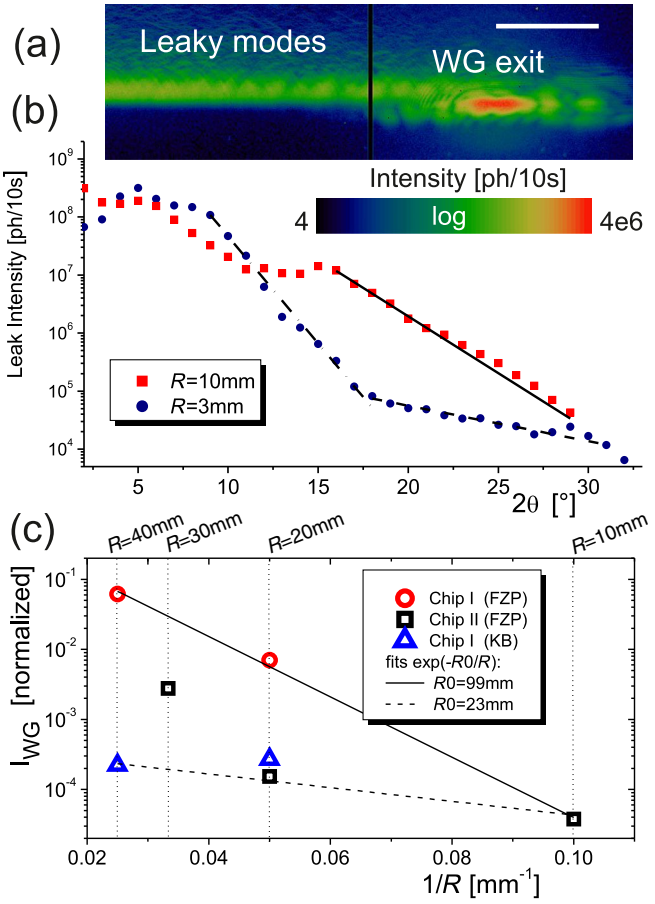

FIG. 3 (color online). Radiation loss and waveguide exit flux. (a) High-resolution far-field intensity distribution (logarithmically scaled color code) around the horizon of the $R = 40$ mm channel exit at $\theta_{WG} = 7.12°$ (red colored intensity maximum in right detector panel) with a total waveguide exit intensity $I_{WG} = 0.97 \times 10^8$ ph/s, as computed from the corresponding region of interest in the right detector panel. A fine structure in the leakage radiation (horizontal stripe) is observed, originating from interference of radiation tunneling out of the leaky modes. Scale bar: 100 pixel, corresponding to 5.5 mm on the detector, or $\Delta\theta = 0.42°$. (b) Integrated leakage intensity along the contour as a function of θ for different channels (not including the WG exit radiation). (c) Waveguide exit intensities as a function of $1/R$, normalized to the flux impinging onto the channel entrance, along two exponential curves $\exp(-R_0/R)$ as a guide to the eye, with $R_0 = 99$ mm (solid line) and $R_0 = 23$ mm, respectively. Note that in order to obtain the correct transmission of the channels, these values have to be corrected for coupling efficiency and leakage due to the open top (see Ref. [20]).

impinging on the channel entrance. Systematic differences between the two fabricated XWGchips and between the two coupling conditions, as well as the extremely high sensitivity to even slight misalignment due to the open top of the channels, easily obscure the underlying relationship (see Ref. [20]). However, as an estimate we can conclude from the maximum envelope of the measured data points in the $I_{WG}(1/R)$ plot, indicated as a guide to the eye by the $\exp(-99\ \text{mm}/R)$ curve (solid line). To reliably achieve such transmission values, and to become more tolerant to slight angular misalignment, radiation should be prevented from coupling out vertically in the future, using wafer bonding techniques to cap the channels [15].

In summary, we have investigated within which limits radiation can be transported in curved x-ray waveguides. While curvature is a standard function of visible light optical fibers, the extremely small critical angles in x-ray waveguide optics are commonly considered to impede propagation in curved waveguides. Here, we have overcome this simplistic picture by demonstrating that guiding of hard x-ray radiation is possible with radius of curvature down to $R = 10$ mm, and up to 30° deflection angles (radiation exiting the end of the chip). Experimentally, this was achieved by combination of small channels with a width of $w = 100$ nm and efficient prefocusing optics. Radiation coupled out of the curved channels indicates the leaky nature of the modes. The present experimental configuration with uncapped channels can be further improved by capping the channels by wafer bonding [15], as well as by replacing Ta with a less absorbing cladding [20]. Already for the present system, the curvature dependence of the waveguide exit radiation shows that waveguide-based x-ray optics "on a chip" can be realized with tolerable curvature-induced losses for $R \geq 100$ mm, well suited for applications as splitters, delay lines, or for interferometry and holography applications with multiple beams. One may speculate that guiding even for $R \simeq 1$ mm with 90° or even 180° deflection may become possible for optimum combinations of materials and photon energy.

We thank Michael Sprung for excellent support at the P10 beam line, Martin Krenkel and Anna-Lena Robisch for help during the beamtime, and Lars Melchior and Phillip Höhne for help in numerical simulations. Funding by the German Research Foundation (Deutsche Forschungsgemeinschaft, DFG) through SFB 755 is gratefully acknowledged.

[1] A. Sakdinawat and D. Attwood, Nat. Photonics **4**, 840 (2010).
[2] J. Stangl, C. Mocuta, V. Chamard, and D. Carbone, *Nanobeam X-ray Scattering* (Wiley-VCN, Weinheim, 2014).
[3] C. M. Günther *et al.*, Nat. Photonics **5**, 99 (2011).
[4] Y. Shvyd'ko, *X-ray Optics* (Springer, Berlin, 2004).
[5] C. David *et al.*,Sci. Rep. **5**, 7644 (2015).
[6] W. Roseker, H. Franz, H. Schulte-Schrepping, A. Ehnes, O. Leupold, F. Zontone, A. Robert, and G. Grübel, Opt. Lett. **34**, 1768 (2009).
[7] K. A. Nugent, Adv. Phys. **59**, 1 (2010).
[8] D. Paganin, *Coherent X-Ray Optics* (Oxford University Press, Oxford, 2006).
[9] C. Fuhse, C. Ollinger, and T. Salditt, Phys. Rev. Lett. **97**, 254801 (2006).

[10] M. J. Zwanenburg, J. F. Peters, J. H. H. Bongaerts, S. A. de Vries, D. L. Abernathy, and J. F. van der Veen, Phys. Rev. Lett. **82**, 1696 (1999).
[11] S. DiFonzo, W. Jark, S. Lagomarsino, C. Giannini, L. De Caro, A. Cedola, and M. Müller, Nature (London) **403**, 638 (2000).
[12] I. Bukreeva, A. Popov, D. Pelliccia, A. Cedola, S. B. Dabagov, and S. Lagomarsino, Phys. Rev. Lett. **97**, 184801 (2006).
[13] F. Pfeiffer, C. David, M. Burghammer, C. Riekel, and T. Salditt, Science **297**, 230 (2002).
[14] A. Jarre, C. Fuhse, C. Ollinger, J. Seeger, R. Tucoulou, and T. Salditt, Phys. Rev. Lett. **94**, 074801 (2005).
[15] H. Neubauer, S. Hoffmann, M. Kanbach, J. Haber, S. Kalbfleisch, S. P. Krüger, and T. Salditt, J. Appl. Phys. **115**, 214305 (2014).
[16] M. Bartels, M. Krenkel, J. Haber, R. N. Wilke, and T. Salditt, Phys. Rev. Lett. **114**, 048103 (2015).
[17] C. Liu and J. A. Golovchenko, Phys. Rev. Lett. **79**, 788 (1997).
[18] M. Osterhoff and T. Salditt, Opt. Commun. **282**, 3250 (2009).
[19] T. Salditt, M. Osterhoff, M. Krenkel, R. N. Wilke, M. Priebe, M. Bartels, S. Kalbfleisch, and M. Sprung, J. Synchrotron Radiat. **22**, 867 (2015).
[20] See Supplemental Material at http://link.aps.org/supplemental/10.1103/PhysRevLett.115.203902, which includes Refs. [22–23], for more details on the experiment and numerical simulations.
[21] M. Heiblum and J. H. Harris, IEEE J. Quantum Electron. **11**, 75 (1975).
[22] C. Bergemann, H. Keymeulen, and J. F. van der Veen, Phys. Rev. Lett. **91**, 204801 (2003).
[23] C. Fuhse and T. Salditt, Opt. Commun. **265**, 140 (2006).